

See discussions, stats, and author profiles for this publication at: <https://www.researchgate.net/publication/5298356>

Probing the Electronic Structure and Chemical Bonding of Gold Oxides and Sulfides in AuO_n – and AuS_n – ($n = 1, 2$)

ARTICLE in JOURNAL OF THE AMERICAN CHEMICAL SOCIETY · AUGUST 2008

Impact Factor: 12.11 · DOI: 10.1021/ja802408b · Source: PubMed

CITATIONS

49

READS

36

4 AUTHORS, INCLUDING:



Lai-Sheng Wang

Brown University

434 PUBLICATIONS 18,822 CITATIONS

SEE PROFILE

Probing the Electronic Structure and Chemical Bonding of Gold Oxides and Sulfides in AuO_n^- and AuS_n^- ($n = 1, 2$)Hua-Jin Zhai,[†] Christian Bürgel,[‡] Vlasta Bonacic-Koutecky,^{*,‡} and
Lai-Sheng Wang^{*,†}

Department of Physics, Washington State University, 2710 University Drive, Richland,
Washington 99354, Chemical & Materials Sciences Division, Pacific Northwest National
Laboratory, MS K8-88, P.O. Box 999, Richland, Washington 99352, and Humboldt Universität
zu Berlin, Institut für Chemie, Brook-Taylor Straße 2, D-12489 Berlin, Germany

Received April 2, 2008; E-mail: vbk@chemie.hu-berlin.de; ls.wang@pnl.gov

Abstract: The Au–O and Au–S interactions are essential in nanogold catalysis and nanotechnology, for which monogold oxide and sulfide clusters serve as the simplest molecular models. We report a combined photoelectron spectroscopy and *ab initio* study on AuO^- and AuO_2^- and their valent isoelectronic AuS^- and AuS_2^- species to probe their electronic structure and to elucidate the Au–O and Au–S chemical bonding. Vibrationally resolved spectra were obtained at different photon energies, providing a wealth of electronic structure information for each species. Similar spectra were observed for AuO^- and AuS^- and for the linear OAuO^- and SAuS^- species. A bent isomer was also observed as $\text{Au}(\text{S}_2)^-$ in the AuS_2^- spectra, whereas a similar $\text{Au}(\text{O}_2)^-$ complex was not observed in the case of AuO_2^- . High-level *ab initio* calculations were conducted to aid spectral assignments and provide insight into the chemical bonding in the AuX^- and AuX_2^- molecules. Excellent agreement is achieved between the calculated electronic excitations and the observed spectra. Configuration interactions and spin–orbit couplings were shown to be important and were necessary to achieve good agreement between theory and experiment. Strong covalent bonding was found in both the AuX^- and the XAuX^- species with multiple bonding characters. While $\text{Au}(\text{S}_2)^-$ was found to be a low-lying isomer with a significant binding energy, $\text{Au}(\text{O}_2)^-$ was shown to be unbound consistent with the experimental observation. The latter is understood in the context of the size-dependent reactivity of Au_n^- clusters with O_2 .

1. Introduction

Gold is the noblest of all metals and does not form very stable oxides.^{1–6} The discovery of unique catalytic properties of nanosized gold particles, in particular for CO oxidation at low temperatures,^{7–9} has motivated a recent surge of research activity in gold oxide clusters.^{10–20} Despite extensive research efforts, the exact mechanisms of the nanocatalytic effects of gold are still controversial.^{7,8} Gas-phase experimental studies in combination with high-level theoretical calculations may provide fundamental insights into nanogold catalysis and have been actively pursued.^{10–15,21–23} Monogold oxide species may be considered as the simplest model system relevant to nanogold catalytic CO oxidation. Indeed, Au atom based CO oxidation at a temperature as low as 10 K was demonstrated in 1977.²⁴

Monogold oxide clusters have been the subject of numerous matrix experimental studies.^{1–6} An earlier electronic emission spectrum in a neon matrix reported a vibrational frequency of 699 cm^{-1} for AuO^- .² A subsequent matrix experiment in argon, however, reported frequencies at 619.2 and 586.9 cm^{-1} , which were assigned to the $^{16}\text{O}/^{18}\text{O}$ isotopic species of AuO , respectively.⁵ A gold dioxygen complex $\text{Au}(\text{O}_2)$ was also reported in

[†] Washington State University and Pacific Northwest National Laboratory.[‡] Humboldt Universität zu Berlin.

- (1) McIntosh, D.; Ozin, G. A. *Inorg. Chem.* **1976**, *15*, 2869.
- (2) Griffiths, M. J.; Barrow, R. F. *J. Chem. Soc., Faraday Trans.* **1977**, *73*, 943.
- (3) Howard, J. A.; Sutcliffe, R.; Mile, B. *J. Phys. Chem.* **1984**, *88*, 4351.
- (4) Kasai, P. H.; Jones, P. M. *J. Phys. Chem.* **1986**, *90*, 4239.
- (5) Citra, A.; Andrews, L. *THEOCHEM* **1999**, 489, 95.
- (6) Wang, X.; Andrews, L. *J. Phys. Chem. A* **2001**, *105*, 5812.
- (7) (a) Haruta, M. *Catal. Today* **1997**, *36*, 153. (b) Bond, G. C.; Thompson, D. T. *Catal. Rev. Sci. Eng.* **1999**, *41*, 319. (c) Haruta, M. *Chem. Rec.* **2003**, *3*, 75. (d) Meyer, R.; Lemire, C.; Shaikhutdinov, S. K.; Freund, H. J. *Gold Bull.* **2004**, *37*, 72.
- (8) Cho, A. *Science* **2003**, *299*, 1684.

- (9) For selected surface studies, see: (a) Valden, M.; Lai, X.; Goodman, D. W. *Science* **1998**, *281*, 1647. (b) Chen, M. S.; Goodman, D. W. *Science* **2004**, *306*, 252. (c) Chen, M.; Kumar, D.; Goodman, D. W. *Science* **2005**, *310*, 291. (d) Sanchez, A.; Abbet, S.; Heiz, U.; Schneider, W. D.; Hakkinen, H.; Barnett, R. N.; Landman, U. *J. Phys. Chem. A* **1999**, *103*, 9573. (e) Yoon, B.; Hakkinen, H.; Landman, U.; Worz, A. S.; Antonietti, J.-M.; Abbet, S.; Judai, K.; Heiz, U. *Science* **2005**, *307*, 403. (f) Kim, T. S.; Stiehl, J. D.; Reeves, C. T.; Meyer, R. J.; Mullins, C. B. *J. Am. Chem. Soc.* **2003**, *125*, 2018. (g) Stiehl, J. D.; Kim, T. S.; McClure, S. M.; Mullins, C. B. *J. Am. Chem. Soc.* **2004**, *126*, 1606. (h) Lee, S.; Fan, C.; Wu, T.; Anderson, S. L. *J. Am. Chem. Soc.* **2004**, *126*, 5682. (i) Guzman, J.; Gates, B. C. *J. Am. Chem. Soc.* **2004**, *126*, 2672. (j) Date, M.; Okumura, M.; Tsubota, S.; Haruta, M. *Angew. Chem., Int. Ed.* **2004**, *43*, 2129. (k) Lemire, C.; Meyer, R.; Shaikhutdinov, S.; Freund, H. J. *Angew. Chem., Int. Ed.* **2004**, *43*, 118. (l) Deng, X.; Min, B. K.; Guloy, A.; Friend, C. M. *J. Am. Chem. Soc.* **2005**, *127*, 9267. (m) Sterrer, M.; Yulikov, M.; Risse, T.; Freund, H.-J.; Carrasco, J.; Illas, F.; Di Valentin, C.; Giordano, L.; Pacchioni, G. *Angew. Chem., Int. Ed.* **2006**, *45*, 2633. (n) Sterrer, M.; Yulikov, M.; Fischbach, E.; Heyde, M.; Rust, H. P.; Pacchioni, G.; Risse, T.; Freund, H.-J. *Angew. Chem., Int. Ed.* **2006**, *45*, 2630. (o) Matthey, D.; Wang, J. G.; Wendt, S.; Matthiesen, J.; Schaub, R.; Lægsgaard, E.; Hammer, B.; Besenbacher, F. *Science* **2007**, *315*, 1692.

matrix experiments and a side-on structure (C_{2v}) was proposed, in which the two O atoms are equivalently coordinated to Au.^{1,3–5} However, a recent matrix study concluded that $\text{Au}(\text{O}_2)$ possesses two inequivalent oxygen atoms and should take a bent structure (C_s).⁶ A linear OAuO ($D_{\infty h}$, gold dioxide) species was also identified.^{5,6}

In the gas phase, the electronic structures of AuO^- and AuO_2^- and their neutrals have not been studied experimentally until very recently.^{13,14,17–19} Gantefor and co-workers conducted a photoelectron spectroscopy (PES) study on AuO^- in 2004 at 193 nm.¹⁴ At about the same time, Lineberger and co-workers¹⁷ reported a highly resolved photoelectron spectrum of AuO^- , as well as AuS^- , at 364 nm for the ground-state transition, clearly resolving the two spin–orbit component for the ground-state of AuO and AuS ($^2\Pi_{3/2,1/2}$). Simultaneously, O'Brien et al.¹⁸ reported a near-infrared electronic spectrum of the $^4\Sigma^-$ excited state of AuO . More recently, Okabayashi et al.^{19a} reported a pure rotational spectrum of the $^2\Pi_{3/2}$ ground state of AuO . Little spectroscopic information is available for other excited states of AuO . Gantefor and co-workers also obtained the photoelectron spectra of AuO_2^- .^{13,14} To the best of our knowledge, there are no other spectroscopic studies on the gold

dioxide species except a recent PES report by Bowen and co-workers^{19b} on AuOH^- and $\text{Au}(\text{H}_2\text{O})_{1,2}^-$. Theoretical studies on the monogold oxides have also been relatively scarce.^{5,6,14,16,18b,25}

The valent isoelectronic monogold sulfide species, AuS_n and AuS_n^- ($n = 1, 2$), have received even less attention. Very few spectroscopic data are available except for the recent study of AuS^- by Lineberger and co-workers along with that of AuO^- .¹⁷ However, the Au–S bonding is important not only for the purpose of comparison to the corresponding Au–O system but also in self-assembled monolayers,²⁶ in which the Au–S bonding plays an important role.

We have been interested in developing cluster models for nanogold catalysis at the molecular level.^{15,23} In the current contribution, we report a comprehensive PES study of AuO^- and AuO_2^- and their isoelectronic AuS^- and AuS_2^- species at 355, 266, and 193 nm photon energies, in combination with high-level *ab initio* calculations. The concerted experimental and computational study allows a complete understanding of the equilibrium geometries, electronic structure, and chemical bonding in these systems. Both a linear SAuS^- and a bent $\text{Au}(\text{S}_2)^-$ species were observed for AuS_2^- , whereas only a linear OAuO^- species was observed for AuO_2^- . This observation is in agreement with our theoretical prediction that Au^- and O_2 is not bound in $\text{Au}(\text{O}_2)^-$, whereas S_2 is bound to Au^- by 1.388 eV in $\text{Au}(\text{S}_2)^-$. Molecular orbital analyses were carried out to obtain insight into the nature of the chemical bonding in the AuX^- diatomics and the AuX_2^- systems. Strong covalent bonding with multibonding characters was found for both systems. The nonbonding nature of the $\text{Au}(\text{O}_2)^-$ complex is understood from the size-dependent reactivity of Au_n^- clusters with O_2 .

2. Experimental and Computational Methods

2.1. Photoelectron Spectroscopy. The experiments were carried out using a magnetic-bottle-type PES apparatus equipped with a laser vaporization supersonic cluster source.²⁷ Briefly, the AuO^- and AuO_2^- anions were produced by laser vaporization of a pure Au target in the presence of a helium carrier gas seeded with either 1% N_2O or 0.5% O_2 as the oxygen source, whereas the AuS^- and AuS_2^- anions were produced with an $\text{Au}_2\text{S}/\text{Au}$ mixed target in the presence of a pure helium carrier gas. The N_2O -seeded helium appears to be a superior oxygen source and seems to produce colder oxide clusters than the O_2 source, as shown in our recent work.²⁸ Cluster temperature control has been shown previously to be essential for obtaining high quality PES data.²⁹ Therefore, all PES data presented here for AuO^- and AuO_2^- were obtained using the 1% N_2O -seeded helium carrier gas. Negatively charged clusters were mass-analyzed using a time-of-flight mass spectrometer, and the species of current interest AuX_n^- ($\text{X} = \text{O}, \text{S}; n = 1, 2$) were each mass-selected and decelerated before being photodetached.

- (10) (a) Lee, T.; Ervin, K. M. *J. Phys. Chem.* **1994**, *98*, 10023. (b) Cox, D. M.; Brickman, R.; Creegan, K.; Kaldor, A. *Z. Phys. D* **1991**, *19*, 353.
- (11) (a) Salisbury, B. E.; Wallace, W. T.; Whetten, R. L. *Chem. Phys.* **2000**, *262*, 131. (b) Wallace, W. T.; Whetten, R. L. *J. Am. Chem. Soc.* **2002**, *124*, 7499.
- (12) (a) Hagen, J.; Socaciu, L. D.; Elijażyfer, M.; Heiz, U.; Bernhardt, T. M.; Woste, L. *Phys. Chem. Chem. Phys.* **2002**, *4*, 1707. (b) Socaciu, L. D.; Hagen, J.; Bernhardt, T. M.; Woste, L.; Heiz, U.; Hakkinen, H.; Landman, U. *J. Am. Chem. Soc.* **2003**, *125*, 10437.
- (13) (a) Stolicic, D.; Fischer, M.; Gantefor, G.; Kim, Y. D.; Sun, Q.; Jena, P. *J. Am. Chem. Soc.* **2003**, *125*, 2848. (b) Kim, Y. D.; Fischer, M.; Gantefor, G. *Chem. Phys. Lett.* **2003**, *377*, 170.
- (14) Sun, Q.; Jena, P.; Kim, Y. D.; Fischer, M.; Gantefor, G. *J. Chem. Phys.* **2004**, *120*, 6510.
- (15) (a) Wallace, W. T.; Wyrwas, R. B.; Whetten, R. L.; Mitric, R.; Bonacic-Koutecky, V. *J. Am. Chem. Soc.* **2003**, *125*, 8408. (b) Kimble, M. L.; Castleman, A. W., Jr.; Mitric, R.; Bürgel, C.; Bonacic-Koutecky, V. *J. Am. Chem. Soc.* **2004**, *126*, 2526. (c) Kimble, M. L.; Moore, N. A.; Johnson, G. E.; Castleman, A. W., Jr.; Bürgel, C.; Mitric, R.; Bonacic-Koutecky, V. *J. Chem. Phys.* **2006**, *125*, 204311. (d) Mitric, R.; Bürgel, C.; Bonacic-Koutecky, V. *Proc. Natl. Acad. Sci. U.S.A.* **2007**, *104*, 10314.
- (16) Okumura, M.; Kitagawa, Y.; Haruta, M.; Yamaguchi, K. *Chem. Phys. Lett.* **2001**, *346*, 163.
- (17) Ichino, T.; Gianola, A. J.; Andrews, D. H.; Lineberger, W. C. *J. Phys. Chem. A* **2004**, *108*, 11307.
- (18) (a) O'Brien, L. C.; Hardimon, S. C.; O'Brien, J. J. *J. Phys. Chem. A* **2004**, *108*, 11302. (b) O'Brien, L. C.; Oberlink, A. E.; Roos, B. O. *J. Phys. Chem. A* **2006**, *110*, 11954.
- (19) (a) Okabayashi, T.; Koto, F.; Tsukamoto, K.; Yamazaki, E.; Tanimoto, M. *Chem. Phys. Lett.* **2005**, *403*, 223. (b) Zheng, W.; Li, X.; Eustis, S.; Grubisic, A.; Thomas, O.; Clercq, H. d.; Bowen, K. *Chem. Phys. Lett.* **2007**, *444*, 232.
- (20) (a) Hakkinen, H.; Landman, U. *J. Am. Chem. Soc.* **2001**, *123*, 9704. (b) Lopez, N.; Norskov, J. K. *J. Am. Chem. Soc.* **2002**, *124*, 11262. (c) Varganov, S. A.; Olson, R. M.; Gordon, M. S.; Metiu, H. *J. Chem. Phys.* **2003**, *119*, 2531. (d) Molina, L. M.; Hammer, B. *Phys. Rev. Lett.* **2003**, *90*, 206102. (e) Yoon, B.; Hakkinen, H.; Landman, U. *J. Phys. Chem. A* **2003**, *107*, 4066. (f) An, W.; Pei, Y.; Zeng, X. C. *Nano Lett.* **2008**, *8*, 195.
- (21) (a) Fielicke, A.; von Helden, G.; Meijer, G.; Pedersen, D. B.; Simard, B.; Rayner, D. M. *J. Am. Chem. Soc.* **2005**, *127*, 8416. (b) Fielicke, A.; von Helden, G.; Meijer, G.; Simard, B.; Rayner, D. M. *J. Phys. Chem. B* **2005**, *109*, 23935.
- (22) (a) Neumaier, M.; Weigend, F.; Hampe, O.; Kappes, M. M. *J. Chem. Phys.* **2005**, *122*, 104702. (b) Neumaier, M.; Weigend, F.; Hampe, O.; Kappes, M. M. *J. Chem. Phys.* **2006**, *125*, 104308.
- (23) (a) Zhai, H. J.; Wang, L. S. *J. Chem. Phys.* **2005**, *122*, 051101. (b) Zhai, H. J.; Kiran, B.; Dai, B.; Li, J.; Wang, L. S. *J. Am. Chem. Soc.* **2005**, *127*, 12098.
- (24) Huber, H.; McIntosh, D.; Ozin, G. A. *Inorg. Chem.* **1977**, *16*, 975.

- (25) Schwerdtfeger, P.; Dolg, M.; Schwarz, W. H. E.; Bowmaker, G. A.; Boyd, P. D. W. *J. Chem. Phys.* **1989**, *91*, 1762.
- (26) Love, J. C.; Estroff, L. A.; Kriebel, J. K.; Nuzzo, R. G.; Whitesides, G. M. *Chem. Rev.* **2005**, *105*, 1103.
- (27) (a) Wang, L. S.; Cheng, H. S.; Fan, J. J. *J. Chem. Phys.* **1995**, *102*, 9480. (b) Wang, L. S.; Wu, H. In *Advances in Metal and Semiconductor Clusters, Vol. 4, Cluster Materials*; Duncan, M. A., Ed.; JAI Press: Greenwich, CT, 1998; pp 299–343.
- (28) Zhai, H. J.; Wang, L. S. *J. Chem. Phys.* **2006**, *125*, 164315.
- (29) (a) Wang, L. S.; Li, X. In *Clusters and Nanostructure Interfaces*; Jena, P.; Khanna, S. N.; Rao, B. K., Eds.; World Scientific: NJ, 2000; pp 293–300. (b) Wang, L. S.; Li, X.; Zhang, H. F. *J. Chem. Phys.* **2000**, *262*, 53. (c) Akola, J.; Manninen, M.; Hakkinen, H.; Landman, U.; Li, X.; Wang, L. S. *Phys. Rev. B* **1999**, *60*, R11297. (d) Zhai, H. J.; Wang, L. S.; Alexandrova, A. N.; Boldyrev, A. I. *J. Chem. Phys.* **2002**, *117*, 7917.

Table 1. Summary of the Ground State Properties Obtained at the CCSD(T) Level of Theory for $\text{AuX}_{1,2}^-$ ($\text{X} = \text{O}, \text{S}$)^a

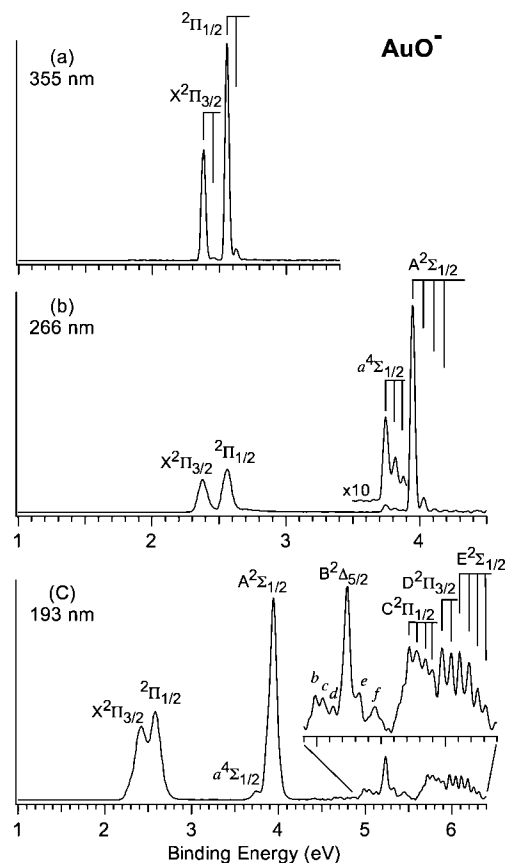
	state	ΔE	$r_{\text{Au-X}}$	$r_{\text{X-X}}$	$D_e(\text{X})^b$	$D_e(\text{X}_2)^c$	VDE
AuO^-	$C_{\infty v}$ $^1\Sigma^+$	-	1.882		2.082		2.312
OAuO^-	$D_{\infty h}$ $^3\Sigma_g^-$	0.000	1.847		4.046		3.473
AuOO^-	C_s $^3A''$	1.421	2.169	1.314	2.626	-0.272	2.058
AuS^-	$C_{\infty v}$ $^1\Sigma^+$	-	2.216		2.677		2.452
SAuS^-	$D_{\infty h}$ $^3\Sigma_g^-$	0.000	2.202		3.388		3.468
AuSS^-	C_s $^1A'$	0.568	2.301	2.030	2.820	1.388	2.282

^a Spatial and electronic symmetry of the ground state species and relative energies (ΔE) of isomers, as well as calculated equilibrium bond lengths ($r_{\text{Au-X}}$ and $r_{\text{X-X}}$) are given. Calculated dissociation energies (D_e) for X atom and X_2 group and the first vertical detachment energy (VDE) from each species are also given. All energies are given in eV, and bond lengths are in Å. ^b Dissociation energy for the most stable fragments regardless of spin, defined as $E(\text{AuX}_{n-1}^-) + E(\text{X})$ with $n = 1, 2$ and $\text{X} = \text{O}, \text{S}$. ^c Dissociation energy of molecularly bound X_2 ($\text{X} = \text{O}, \text{S}$) to Au^- is defined as $E(\text{AuX}_2^-) - [E(\text{Au}^-) + E(\text{X}_2)]$.

Three detachment photon energies were used in the current study: 355 nm (3.496 eV), 266 nm (4.661 eV), and 193 nm (6.424 eV). Photoelectrons were collected at nearly 100% efficiency by the magnetic bottle and analyzed in a 3.5 m long electron flight tube. The photoelectron spectra were calibrated using the known spectra of Au^- and Rh^- , and the energy resolution of the apparatus was $\Delta E_k/E_k \approx 2.5\%$, that is, ~ 25 meV for 1 eV electrons.

2.2. Theoretical Methods. Ground state properties of the anionic species AuX_n^- ($\text{X} = \text{O}, \text{S}$; $n = 1, 2$) were determined using the coupled-cluster level of theory with explicit inclusion of single and double excitations and perturbative treatment of triple excitations [CCSD(T)], as summarized in Table 1. For closed-shell species, a restricted HF wave function was used as reference, and for open-shell systems high spin restricted open-shell HF wave functions were employed. Relativistic effects were taken into account by using a scalar-relativistic effective 19-electron core potential for gold (ECP60MDF)³⁰ in combination with the aug-cc-pVTZ-PP AO basis set ((11s10p9d3f2g)/[6s6p5d3f2g]).³¹ The standard aug-cc-pVTZ-PP AO basis set was used for oxygen ((11s,6p,3d,2f)/[5s,4p,3d,2f]) and sulfur ((16s10p3d2f)/[6s5p3d2f]). The energetically lowest orbitals, consisting mainly of Au-(5s, 5p), O-(1s), and S-(1s, 2s, 2p), were frozen. The ground-state geometries of all species were optimized, and properties such as binding energies and vertical detachment energies (VDEs) were determined.

Spin-orbit (SO) interactions were treated by using the contracted SO configuration interaction method after the electron-correlation step, diagonalizing the SO matrix in the space of all SO-free electronic states of interest. For this purpose, the SO-free states for the neutral species in the geometry of the optimized anions were obtained according to the following procedure. First, a state-averaged complete active space self-consistent field (CASSCF) calculation was performed, leading to the following active spaces in which all electrons were correlated: AuO/AuS , 17 orbitals for 10 electrons [CASSCF(17,10)] and $\text{OAuO}/\text{SAuS}/\text{AuSS}$, 23 orbitals for 14 electrons [CASSCF(23,14)]. Since only states with one-electron excitation character dominates the experimental photoelectron spectra, only electronic states with doublet multiplicity are experimentally observable for species in which the anionic electronic ground state is singlet ($\text{AuO}^-/\text{AuS}^-/\text{AuSS}^-$). Within the one-electron approximation, doublet final states $\text{X}(^2\Pi)$, $\text{A}(^2\Sigma)$, $\text{B}(^2\Delta)$, $(^2^2\Sigma)$, and $(^2^2\Pi)$ dominated by one-electron excitations are obtained for AuX ($\text{X} = \text{O}, \text{S}$) by detaching one electron from an orbital of the closed-shell anion AuX^- . These and a few more doublet states with multielectron excitation characters, as well as the lowest $^4\Pi$ and $^4\Sigma$ states, were included in the state-averaged CASSCF. For $\text{Au}(\text{S}_2)$ (C_s , $^2A''$), four $^2A'$ and two $^2A''$ states, which are dominated

**Figure 1.** Photoelectron spectra of AuO^- at (a) 355 nm (3.496 eV), (b) 266 nm (4.661 eV), and (c) 193 nm (6.424 eV). The resolved vibrational structures are labeled with vertical lines.

by one-electron transitions, were included in the state-averaged CASSCF. Additionally, few doublet as well as quartet states representing multielectron excitations were also calculated.

For AuO_2^- ($D_{\infty h}$, $^3\Sigma_g^-$) and AuS_2^- ($D_{\infty h}$, $^3\Sigma_g^-$) with a triplet electronic ground state, both doublet and quadruplet states of the corresponding neutral species are accessible via one-electron detachment processes. Therefore, in calculations for AuO_2 ($D_{\infty h}$, $^2\Pi_g$), the following states were included: $\text{X}(^2\Pi_g)$, $(^2,^4\Pi_u)$, $(^2,^4\Sigma_g^-)$, $(^2,^4\Sigma_u^-)$, $(^4\Delta)$, $(^2^2\Pi_g)$ and a few states with multielectron excitation characters. Analogous states were also considered for AuS_2 ($D_{\infty h}$, $^2\Pi_g$).

Employing the natural orbitals from the state-averaged CAS calculations, we calculated the highly correlated wave functions using the internally contracted MR-CI method. From these, the SO-matrix was constructed and diagonalized, yielding the SO eigenstates. The first peak in a photoelectron spectrum represents the first experimental VDE, thus corresponding to the VDE obtained at the CCSD(T) level of theory. Other higher binding energy peaks in a photoelectron spectrum represent excited states of the neutral species, and their VDEs were computed by adding the excitation energies of the corresponding neutral at the anion geometry to the first VDE. All calculations were performed using the MOLPRO program suite.³²

3. Experimental Results

The photoelectron spectra of AuO^- and AuO_2^- are shown in Figures 1 and 2; those of AuS^- and AuS_2^- are shown in Figures 3 and 4, respectively. The 193 nm spectra of AuO^-

(30) Figgen, D.; Rauhut, G.; Dolg, M.; Stoll, H. *Chem. Phys.* **2005**, *311*, 227.

(31) Peterson, K. A.; Puzzarini, C. *Theor. Chem. Acc.* **2005**, *114*, 283.

(32) Werner, H.-J. et al. *MOLPRO*, version 2006.1, a package of ab initio programs; see <http://www.molpro.net>.

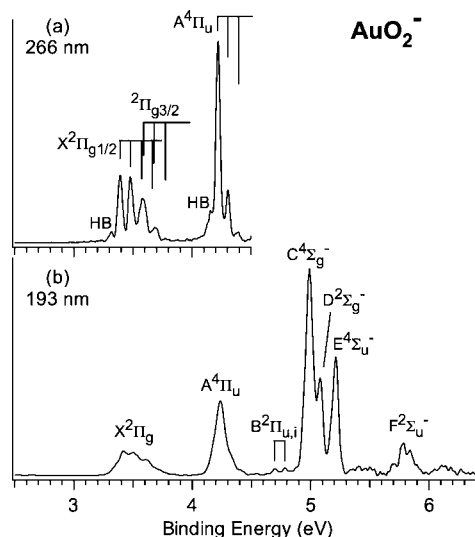


Figure 2. Photoelectron spectra of AuO_2^- at (a) 266 and (b) 193 nm. The resolved vibrational structures at 266 nm are labeled with vertical lines.

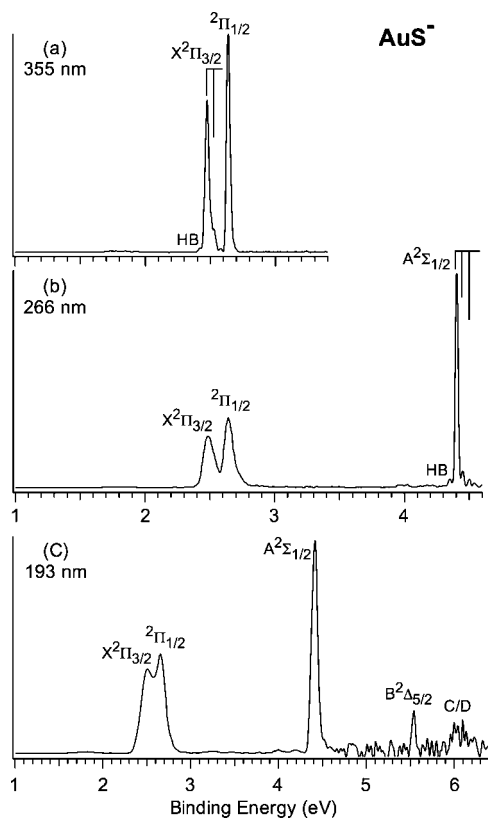


Figure 3. Photoelectron spectra of AuS^- at (a) 355, (b) 266, and (c) 193 nm. The resolved vibrational structures are labeled with vertical lines.

and AuO_2^- are compared with the corresponding sulfide species in Figure S1. The observed electronic transitions and resolved vibrational structures are labeled in Figures 1–4. All the measured adiabatic detachment energies (ADEs), VDEs, and vibrational frequencies are given in Table 2 for AuO^- and AuO_2^- and Table 3 for AuS^- and AuS_2^- . The spectral assignments and interpretations are done with the aid of the *ab initio* calculations, as shown in Tables 4–8, Figures S2–S5, and discussed in section 4.

3.1. AuO^- . At 355 nm (Figure 1a), a well resolved SO doublet was observed for the ground state of AuO ($\text{X}^2\Pi_{3/2,1/2}$).

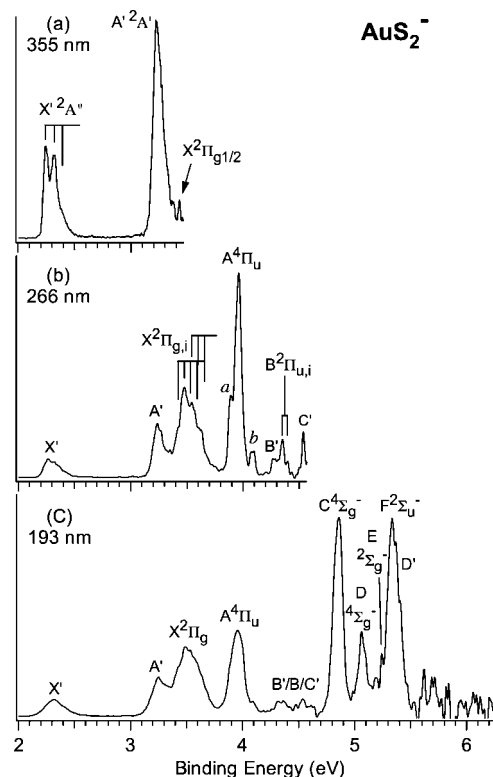


Figure 4. Photoelectron spectra of AuS_2^- at (a) 355, (b) 266, and (c) 193 nm. The resolved vibrational structures are labeled with vertical lines. Note that two isomers are contained in the spectra: $\text{Au}(\text{S}_2)^-$ (X' , A' , B' , ...) and SAuS^- (X , A , B , ...). See text.

Table 2. Observed Adiabatic (ADE) and Vertical (VDE) Detachment Energies for AuO^- ($^1\Sigma^+$) and AuO_2^- ($D_{\infty h}$, $^3\Sigma_g^-$) and Term Values and Vibrational Frequencies for AuO and AuO_2

	feature	ADE (eV) ^a	term value (eV)	VDE (eV) ^a	vib freq (cm ⁻¹) ^a
$\text{AuO}^- (^1\Sigma^+)$	X ($^2\Pi_{3/2}$)	2.378 (15) ^b	0	2.378 (15)	640 (60)
	($^2\Pi_{1/2}$)	2.556 (15)	0.178	2.556 (15)	540 (60)
	a ($^4\Sigma_{1/2}$)	3.745 (20)	1.367	3.745 (20)	530 (50)
	A ($^2\Sigma_{1/2}$)	3.945 (20)	1.567	3.945 (20)	630 (50)
	b	4.99 (3)		4.99 (3)	
	c	5.05 (3)		5.05 (3)	
	d	5.13 (3)		5.13 (3)	
	B ($^2\Delta_{5/2}$)	5.24 (3)	2.86	5.24 (3)	
	e	5.33 (3)		5.33 (3)	
	f	5.45 (3)		5.45 (3)	
$\text{AuO}_2^- (D_{\infty h}, ^3\Sigma_g^-)$	C ($^2\Pi_{1/2}$)	5.72 (4)	3.342	5.72 (4)	480 (50)
	D ($^2\Pi_{3/2}$)	5.97 (4)	3.592	5.97 (4)	560 (50)
	E ($^2\Sigma_{1/2}$)	6.11 (4)	3.732	6.11 (4)	560 (50)
OAuO^-	X ($^2\Pi_{g1/2}$)	3.40 (3) ^b	0	3.40 (3)	740 (60) ^c
	($^2\Pi_{g3/2}$)	3.60 (4)	0.20	3.60 (3)	~740
	A ($^4\Pi_{u,i}$)	4.23 (3)	0.83	4.23 (2)	680 (60) ^c
	B ($^2\Pi_{u1/2}$)	4.70 (4)	1.30	4.70 (4)	
	($^2\Pi_{u3/2}$)	4.78 (4)	1.38	4.78 (4)	
	C ($^4\Sigma_g^-$)	4.99 (3)	1.59	4.99 (3)	
	D ($^2\Sigma_g^-$)	5.08 (3)	1.68	5.08 (3)	
	E ($^4\Sigma_u^-$)	5.21 (3)	1.81	5.21 (3)	
	F ($^2\Sigma_u^-$)	5.79 (4)	2.39	5.79 (4)	

^a Numbers in parentheses represent the experimental uncertainties in the last digits. ^b Electron affinity of the neutral. A slightly more accurate value for AuO was reported in ref 17 (2.374 ± 0.007 eV). ^c The anion ground-state frequency was measured to be 640 ± 40 cm⁻¹ from the hot band transitions.

The 0–0 transition of the $^2\Pi_{3/2}$ component yielded an ADE of 2.378 ± 0.015 eV, which defines the electron affinity (EA) of AuO . A weak vibrational progression was resolved, yielding a

Table 3. Observed Adiabatic (ADE) and Vertical (VDE) Detachment Energies for $\text{AuS}^- (^1\Sigma^+)$ and $\text{AuS}_2^- (D_{\infty h}^{\infty} {}^3\Sigma_g^- \text{ and } C_s {}^1A')$ and Term Values and Vibrational Frequencies for the Corresponding Neutrals

	feature	ADE (eV) ^a	term value (eV)	VDE (eV) ^a	vib freq (cm ⁻¹)
AuS^-	X (${}^2\Pi_{3/2}$)	2.475 (15) ^b	0	2.475 (15)	410 (50)
	(${}^2\Pi_{1/2}$)	2.637 (15)	0.162	2.637 (15)	
	A (${}^2\Sigma_{1/2}$) ^c	4.402 (15)	1.927	4.402 (15)	400 (60)
	B (${}^2\Delta_{5/2}$)	5.54 (3)	3.069	5.54 (3)	
	C/D	~6.1		~6.1	
SAuS^- ($D_{\infty h}^{\infty} {}^3\Sigma_g^-$)	X (${}^2\Pi_{g1/2}$)	3.42 (3)	0	3.47 (3)	~440
	(${}^2\Pi_{g3/2}$)	3.54 (4)	0.12	3.54 (4)	
	A (${}^4\Pi_{u,i}$)	3.96 (3)	0.54	3.96 (3)	
	B (${}^2\Pi_{u1/2}$)	4.35 (5)	0.93	4.35 (5)	
	(${}^2\Pi_{u3/2}$)	4.40 (5)	0.98	4.40 (5)	
	C (${}^4\Sigma_u^-$)	4.86 (3)	1.44	4.86 (3)	
	D (${}^4\Sigma_g^-$)	5.07 (5)	1.65	5.07 (5)	
	E (${}^2\Sigma_g^-$)	5.24 (6)	1.82	5.24 (6)	
	F (${}^2\Sigma_u^-$)	5.34 (6)	1.92	5.34 (6)	
	X' (${}^2A''$)	2.24 (3)	0	2.24 (3)	~610
$\text{Au(S}_2)_-$ ($C_s, {}^1A'$)	A' (${}^2A'$)	3.22 (3)	0.98	3.22 (3)	
	B' (${}^2A''$)	4.27 (6)	2.03	4.27 (6)	
	C' (${}^2A'$)	4.54 (5)	2.30	4.54 (5)	
	D' (${}^2A''$)	5.40 (5)	3.16	5.40 (5)	

^a Numbers in parentheses represent the experimental uncertainties in the last digits. ^b Electron affinity of the neutral. A previous value for AuS is 2.469 ± 0.006 eV (ref 17). ^c anion ground-state as measured from the hot band transition: 430 ± 50 cm⁻¹.

Table 4. Calculated Vertical Detachment Energies (VDE) for AuO^- Compared to the Experimental Values^a

final state	Ω	VDE (eV)		contribution of basis states to SO eigenstates
		theor	expt	
X (${}^2\Pi_{3/2}$)	3/2	2.312	2.378 ± 0.015	97% [${}^1\Sigma_{3/2}$]
(${}^2\Pi_{1/2}$)	1/2	2.464	2.566 ± 0.015	97% [${}^1\Sigma_{1/2}$]
a (${}^4\Sigma_{1/2}$)	1/2	3.797	3.745 ± 0.020	36% [${}^1\Sigma_{1/2}$] + 43% [${}^1\Sigma_{1/2}$] + 18% (${}^4\Pi_{1/2}$)
A (${}^2\Sigma_{1/2}$)	1/2	3.925	3.945 ± 0.020	56% [${}^1\Sigma_{1/2}$] + 38% (${}^4\Sigma_{1/2}$)
B (${}^2\Delta_{5/2}$)	5/2	5.443	5.24 ± 0.03	96% [${}^2\Delta_{5/2}$]
C (${}^2\Pi_{1/2}$)	1/2	5.818	5.72 ± 0.04	12% [${}^2\Sigma_{1/2}$] + 39% (${}^2\Pi_{1/2}$) + 27% (${}^2\Sigma_{1/2}$)
D (${}^2\Pi_{3/2}$)	3/2	6.111	5.97 ± 0.04	57% [${}^2\Pi_{3/2}$] + 17% [${}^2\Delta_{3/2}$] + 13% (${}^2\Pi_{3/2}$)
E (${}^2\Sigma_{1/2}$)	1/2	6.248	6.11 ± 0.04	61% [${}^2\Sigma_{1/2}$] + 21% [${}^2\Pi_{1/2}$]

^a Symmetries of excited states with dominant single excitation corresponding to experimentally allowed states are given in square brackets; labels for forbidden states with contributions from multiple excitations are given in round brackets.

frequency of 640 ± 60 cm⁻¹ for the ${}^2\Pi_{3/2}$ ground state of AuO. The ADE of the ${}^2\Pi_{1/2}$ component was measured to be 2.556 eV, yielding an SO splitting of 0.178 eV. The resolved vibrational feature yielded a frequency of 540 ± 60 cm⁻¹ for the ${}^2\Pi_{1/2}$ state. The current 355 nm spectrum is consistent with the previous PES study at 364 nm,¹⁷ which was taken at a higher resolution, yielding a more accurate EA (2.374 ± 0.007 eV). However, the previous spectrum did not produce a vibrational frequency for the ${}^2\Pi_{3/2}$ ground state due to the weak $1 \leftarrow 0$ vibrational transition. The good signal-to-noise ratio of the current data allowed the vibrational frequency to be estimated for the ${}^2\Pi_{3/2}$ ground state. The obtained value 640 ± 60 cm⁻¹ is consistent with a recent microwave spectroscopic study, which yielded a much more accurate frequency (624.6 ± 0.2 cm⁻¹) for the ${}^2\Pi_{3/2}$ ground state of AuO.^{19a} It should be noted that the spectrum of AuO^- reported in ref 14 did not resolve the SO components for the ${}^2\Pi$ ground state, and the peak position also appeared to be off by a large amount.

The 266 nm spectrum (Figure 1b) revealed two excited states for AuO each with a well resolved vibrational progression. The very weak progression ($a' {}^2\Sigma_{1/2}$) at 3.745 eV has a vibrational frequency of 530 ± 50 cm⁻¹. The dominant feature in the 266 nm spectrum is the intense band A (${}^2\Sigma_{1/2}$) at 3.945 eV with a vibrational frequency of 630 ± 50 cm⁻¹. At 193 nm (Figure 1c), numerous features were observed above 5 eV. The assignments of these features were aided by the *ab initio* calculations, as labeled in Figure 1c and given in detail in Table 4, as well as shown in Figure S2. The VDEs and ADEs of all the observed PES features for AuO^- are summarized in Table 2.

3.2. AuO_2^- . Two vibrationally resolved bands X and A were observed for AuO_2^- at 266 nm (Figure 2a). The ground-state band X consists of six peaks due to vibrational fine features. The lowest binding energy peak (labeled as HB) is assigned to a hot band transition, yielding a vibrational frequency for the ground state of AuO_2^- as ~ 600 cm⁻¹. The most intense peak at 3.40 eV represents the 0–0 transition and defines the EA for AuO_2 . The spacing between the second and third peaks defines a ground-state vibrational frequency of 740 ± 60 cm⁻¹ for the AuO_2 neutral. The fourth and fifth peaks are broader than the first three peaks, and they appear to have contributions from an unresolved overlapping vibrational progression, as labeled in Figure 2a. As will be discussed in section 4, the ground state of AuO_2 ($D_{\infty h}$) is ${}^2\Pi_g$ and this group of peaks represents two vibrational progressions due to the SO splitting (${}^2\Pi_{g1,2,3/2}$). The origin of the ${}^2\Pi_{g3/2}$ component was estimated to be at 3.60 eV, yielding a SO splitting of 0.20 eV (Table 2). At higher binding energies, a more intense excited-state band ($A' {}^4\Pi_u$) was well resolved, containing a hot band transition (HB) and a short vibrational progression with a spacing of 680 ± 60 cm⁻¹.

The 193 nm spectrum (Figure 2b) of AuO_2^- revealed numerous transitions to higher excited states of AuO_2 . The ADEs and VDEs of these bands are summarized in Table 2, and their assignments, as shown in Figure 2, are given in Table 6, where they are compared to the *ab initio* calculations (also see Figure S4). The current spectra of AuO_2^- are better resolved than the previous PES study,¹³ allowing more accurate spectroscopic information to be obtained. In particular, the previous work did not resolve the SO components of the ground state, and the EA reported for AuO_2 (3.30 eV) appeared to have been derived from the hot band transition. In addition, the B and D bands, as well as the vibrational progression in the A band, were not resolved previously.

3.3. AuS^- . As expected, the spectra of AuS^- (Figure 3) are nearly identical to those of AuO^- (see Figure S1). At 355 nm (Figure 3a), the two SO components (${}^2\Pi_{3/2,1/2}$) for the ground state of AuS were well resolved. The origin of the ${}^2\Pi_{3/2}$ state at 2.475 (± 0.015) eV defines the EA for AuS. A short vibrational progression was resolved for the ${}^2\Pi_{3/2}$ ground state of AuS, yielding a frequency of 410 ± 50 cm⁻¹. A weak hot band transition was also observed for the ${}^2\Pi_{3/2}$ state, yielding a vibrational frequency of 430 ± 60 cm⁻¹ for the ground state of AuS^- . The ${}^2\Pi_{1/2}$ SO component was observed at 2.637 eV, yielding a SO splitting of 0.162 eV. However, there are no vibrational features observed for the ${}^2\Pi_{1/2}$ state beyond the intense 0–0 transition, suggesting that there is no bond length change from the ground state of AuS^- to the ${}^2\Pi_{1/2}$ state of AuS. The current 355 nm spectrum of AuS^- is consistent with the previous study at 364 nm.¹⁷ The higher resolution of the previous work yielded a more accurate EA for AuS ($2.469 \pm$

Table 5. Calculated Vertical Detachment Energies (VDE) for AuS^- Compared to the Experimental Values^a

final state	Ω	VDE (eV)		contribution of basis states to SO eigenstates
		theor	expt	
X ($^2\Pi_{3/2}$)	3/2	2.452	2.475 ± 0.015	98% [$1^2\Pi_{3/2}$]
($^2\Pi_{1/2}$)	1/2	2.562	2.637 ± 0.015	99% [$1^2\Pi_{1/2}$]
a ($^4\Sigma_{1/2}$)	1/2	4.146		9% [$1^2\Sigma_{1/2}$] + 78% ($1^4\Sigma_{1/2}$)
A ($^2\Sigma_{1/2}$)	1/2	4.242	4.402 ± 0.015	87% [$1^2\Sigma_{1/2}$] + 10% ($1^4\Sigma_{1/2}$)
B ($^2\Delta_{5/2}$)	5/2	5.525	5.54 ± 0.03	85% [$2^2\Delta_{5/2}$]
C ($^2\Sigma_{1/2}$)	1/2	6.315	~6.1	32% [$2^2\Sigma_{1/2}$] + 21% ($^2\Pi_{1/2}$) + 21% ($^4\Delta_{1/2}$)
D ($^2\Pi_{3/2}$)	3/2	6.319	~6.1	82% [$2^2\Pi_{3/2}$]
	3/2	7.134		23% [$2^2\Sigma_{3/2}$] + 10% [$2^2\Pi_{3/2}$] + 37% ($^4\Phi_{3/2}$)

^aSymmetries of excited states with dominant single excitation corresponding to experimentally allowed states are given in square brackets; labels for forbidden states with contributions from multiple excitations are given in round brackets.

Table 6. Calculated Vertical Detachment Energies (VDE) for AuO_2^- ($D_{\infty h}$, $^3\Sigma_g^-$) Compared to the Experimental Values^a

final state	Ω	VDE (eV)		contribution of basis states to SO eigenstates
		theor	expt	
X ($^2\Pi_{g1/2}$)	1/2	3.473	3.40 ± 0.03	93% [$1^2\Pi_{g1/2}$]
($^2\Pi_{g3/2}$)	3/2	3.627	3.60 ± 0.04	96% [$1^2\Pi_{g3/2}$]
A ($^4\Pi_{u,i}$)	5/2	4.283	4.23 ± 0.02	99% [$4^4\Pi_{u5/2}$]
	3/2	4.285		94% [$4^4\Pi_{u3/2}$]
	1/2	4.288		96% [$4^4\Pi_{u1/2}$]
	-1/2	4.297		95% [$4^4\Pi_{u-1/2}$]
B ($^2\Pi_{u1/2}$)	1/2	4.713	4.70 ± 0.04	98% [$2^2\Pi_{u1/2}$]
($^2\Pi_{u3/2}$)	3/2	4.785	4.78 ± 0.04	95% [$2^2\Pi_{u3/2}$]
C ($^4\Sigma_g^-$)	3/2	4.939	4.99 ± 0.03	96% [$4^4\Sigma_g^-$]
	1/2	4.964		94% [$4^4\Sigma_g^-$]
D ($^2\Sigma_g^-$)	1/2	5.076	5.08 ± 0.03	96% [$2^2\Sigma_g^-$]
E ($^4\Sigma_u^-$)	3/2	5.341	5.21 ± 0.03	98% [$4^4\Sigma_u^-$]
	1/2	5.343		100% [$4^4\Sigma_u^-$]
F ($^2\Sigma_u^-$)	1/2	6.106	5.79 ± 0.04	97% [$2^2\Sigma_u^-$]
		6.216		11% [$4^4\Delta$] + 88% ($4^4\Pi_g$)
		6.382		31% [$2^4\Pi_g$] + 59% ($4^4\Pi_g$)
		6.612		98% [$4^4\Delta$]

^aSymmetries of excited states with dominant single excitation corresponding to experimentally allowed states are given in square brackets; labels for forbidden states with contributions from multiple excitations are given in round brackets.

0.006 eV) and a more accurate vibrational frequency for the $^2\Pi_{3/2}$ ground state ($400 \pm 30 \text{ cm}^{-1}$).

At 266 nm (Figure 3b), the intense transition to the $A^2\Sigma_{1/2}$ state at 4.402 eV is similar to the same transition in the AuO^- spectrum at 3.945 eV (Figure 1b). The short vibrational progression yields a frequency of $400 \pm 60 \text{ cm}^{-1}$ for the $A^2\Sigma_{1/2}$ state of AuS^- . A hot band feature was also observed in the A band, yielding a ground-state vibrational frequency for AuS^- similar to that from the hot band of the $X^2\Pi_{3/2}$ state (Figure 3a). However, the corresponding $a^4\Sigma_{1/2}$ state was negligible in the 266 nm spectrum of AuS^- , in contrast to that observed in the 266 nm spectrum of AuO^- (Figure 1b). As will be discussed in section 4, the $a^4\Sigma_{1/2}$ state was due to a multielectron transition and configurational mixing with the $^2\Sigma_{1/2}$ state (Tables 4 and 5). The negligible intensity of this multielectron transition in the AuS^- spectrum is consistent with the negligible mixing of the $^2\Sigma_{1/2}$ state (Table 5).

The signal-to-noise ratio of the 193 nm of AuS^- (Figure 3c) was relatively poor, particularly in the higher binding energy range in comparison to the 193 nm spectrum of AuO^- (Figure 1c). In addition to the intense X and A bands, only the $B^2\Delta_{5/2}$

state was well resolved in the high binding energy range. The corresponding transitions to the C and D bands were discernible at ~6.1 eV but were not well resolved in the 193 nm spectrum of AuS^- (Figure 3c).

3.4. AuS_2^- . At first glance, the photoelectron spectra of AuS_2^- (Figure 4) appeared to be rather complicated and totally different from those of the corresponding AuO_2^- (Figure 2). The main differences are the two low binding energy bands (X' and A') observed in the 355 nm spectrum (Figure 4a), which do not exist in the spectra of AuO_2^- . Careful examination shows that, except for the X' and A' bands, most of the spectral features above 3.5 eV at 266 nm (Figure 4b) and 193 nm (Figure 4c) are in fact quite similar to those in the AuO_2^- spectra (see Figure S1). This observation suggests that there are likely two isomers present in the AuS_2^- spectra. Those features above 3.5 eV should correspond mainly to a linear AuS_2^- ($D_{\infty h}$, $^3\Sigma_g^-$) similar to AuO_2^- , whereas the two low binding energy features observed in the 355 nm spectrum should be due to another isomer. As will be shown in section 4, this is indeed the case. The low binding energy features come from a bent $\text{Au}(\text{S}_2)^-$ (C_s , $^1A'$) isomer, which does not exist for AuO_2^- because Au^- and O_2 are unbound (see Table 1).

The X' band was partially vibrationally resolved with a spacing of $\sim 610 \text{ cm}^{-1}$, most likely due to S–S stretching vibrations. The 0–0 transition at 2.24 eV defines the EA for the bent $\text{Au}(\text{S}_2)$ species. The A' band at 3.22 eV represents the first excited state of $\text{Au}(\text{S}_2)$. The width of the A' band suggests that it contains unresolved low-frequency vibrations, probably due to the bending mode. Additional features due to the $\text{Au}(\text{S}_2)^-$ isomer (B' , C' , D') were identified in the 266 and 193 nm spectra with the aid of the theoretical calculations, as given in Table 3 and assigned in Table 8 (also see Figure S5).

The broadband around 3.5 eV is due to the ground-state detachment transition from the linear AuS_2^- ($D_{\infty h}$, $^3\Sigma_g^-$) species. At 266 nm, this band was partially vibrationally resolved with a spacing of $\sim 440 \text{ cm}^{-1}$ for the $X^2\Pi_{g1/2}$ ground state. The 0–0 transition at 3.42 eV, which is well resolved in the 355 nm spectrum (Figure 4a), defines the EA for the linear AuS_2 molecule. The origin for the $^2\Pi_{g3/2}$ SO component was identified at 3.54 eV on the basis of the peak spacings, yielding a SO splitting of 0.12 eV. The intense band at 3.96 eV is due to the first excited state of AuS_2 . The peak labeled *a* could be due to a hot band transition, and peak *b* could not be due to a member of an unresolved vibrational progression of the A band. The ADEs and VDEs of all higher binding energy peaks are given in Table 3, and their assignments shown in Figure 4 are given in Table 7, where they are compared with the *ab initio* data (also see Figure S5).

4. Theoretical Results and Interpretation of the Photoelectron Spectra

4.1. Energetics and Ground State Properties. Table 1 summarizes the ground-state properties of $\text{AuX}_{1,2}^-$ ($X = \text{O}, \text{S}$). The two diatomic species AuX^- are similar, both with a singlet ground state ($^1\Sigma^+$) and similar bond strengths. The Au–S[−] bond (D_e : 2.677 eV) seems slightly stronger than the Au–O[−] bond (D_e : 2.082 eV). The calculated bond lengths and strengths for AuX^- are consistent with a previous study using a similar level of theory.¹⁷ The calculated first VDEs (or EAs for AuX because the VDEs and ADEs are the same due to small bond length changes between the anion and neutral ground state) for AuX^- (2.312 eV for AuO^- and 2.452 eV for AuS^-) are in excellent

Table 7. Calculated Vertical Detachment Energies (VDE) for AuS_2^- ($D_{\infty h}$, $^3\Sigma_g^-$) Compared to the Experimental Values^a

final state	Ω	VDE (eV)		contribution of basis states to SO eigenstates
		theor	expt	
X ($^2\Pi_{g1/2}$)	1/2	3.468	3.47 ± 0.03	92% [$1^2\Pi_{g1/2}$]
($^2\Pi_{g3/2}$)	3/2	3.585	3.54 ± 0.04	97% [$1^2\Pi_{g3/2}$]
A ($^4\Pi_{u,i}$)	5/2	3.991	3.96 ± 0.03	99% [$^4\Pi_{u5/2}$]
	3/2	3.994		94% [$^4\Pi_{u3/2}$]
	1/2	3.995		96% [$^4\Pi_{u1/2}$]
	-1/2	4.003		95% [$^4\Pi_{u-1/2}$]
B ($^2\Pi_{u1/2}$)	1/2	4.344	4.35 ± 0.05	98% [$^2\Pi_{u1/2}$]
($^2\Pi_{u3/2}$)	3/2	4.405	4.40 ± 0.05	95% [$^2\Pi_{u3/2}$]
C ($^4\Sigma_u^-$)	3/2	4.935	4.86 ± 0.03	99% [$^4\Sigma_{u-3/2}$]
	1/2	4.937		99% [$^4\Sigma_{u-1/2}$]
D ($^4\Sigma_g^-$)	1/2	5.170	5.07 ± 0.05	85% [$^4\Sigma_{g-1/2}$] + 8% ($^4\Pi_u$)
	3/2	5.198		84% [$^4\Sigma_{g3/2}$] + 10% ($^4\Pi_u$)
E ($^2\Sigma_g^-$)	1/2	5.251	5.24 ± 0.06	78% [$^2\Sigma_{g-1/2}$] + 12% ($^4\Pi_u$)
F ($^2\Sigma_u^-$)	1/2	5.476	5.34 ± 0.06	99% [$^2\Sigma_{u-1/2}$]
	3/2	6.006		74% [$2^2\Pi_{g3/2}$]
	1/2	6.160		82% [$2^2\Pi_{g1/2}$]
	7/2	6.480		100% [$^4\Delta_{7/2}$]

^a Symmetries of excited states with dominant single excitation corresponding to experimentally allowed states are given in square brackets; labels for forbidden states with contributions from multiple excitations are given in round brackets.

Table 8. Calculated Vertical Detachment Energies (VDE) for $\text{Au(S}_2\text{)}^-$ (C_s , $^1A'$) Compared to the Experimental Values^a

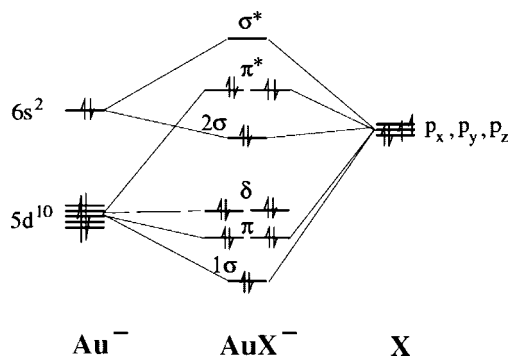
final state	VDE (eV)		contribution of basis states to SO eigenstates
	theor	expt	
X' ($^2A''$)	2.282	2.24 ± 0.03	99% [$1^2A''$]
A' ($^2A'$)	3.013	3.22 ± 0.03	98% [$1^2A'$]
B' ($^2A''$)	4.355	4.27 ± 0.06	64% [$2^2A''$] + 29% [$2^2A'$]
C' ($^2A'$)	4.634	4.54 ± 0.05	29% [$2^2A''$] + 56% [$2^2A'$]
D' ($^2A'$)	5.473	5.40 ± 0.05	33% [$3^2A'$]
	6.186		23% [$3^2A'$] + 44% [$4^2A'$]

^a Symmetries of excited states with dominant single excitation corresponding to experimentally allowed states are given in square brackets.

agreement with the experimental measurements (2.378 ± 0.015 eV for AuO^- and 2.475 ± 0.015 eV for AuS^-).

The most stable structures of the two AuX_2^- species also behave similarly, both possessing a linear XAuX^- structure with a triplet spin state ($^3\Sigma_g^-$). The Au–X bond is significantly strengthened in AuX_2^- relative to the AuX^- diatomics, as can be seen from the shortened Au–X bonds and enhanced dissociation energies in AuX_2^- (Table 1). The calculated first VDEs for AuX_2^- (3.473 eV for AuO_2^- and 3.468 for AuS_2^-) are also in excellent agreement with the experimental measurements (3.40 ± 0.03 eV for AuO_2^- and 3.47 ± 0.03 eV for AuS_2^-).

Interestingly, AuS_2^- is predicted to possess a low-lying isomer containing a molecular S_2 unit with C_s symmetry and a singlet electronic state ($^1A'$). The Au^- and S_2 bonding is quite strong with a dissociation energy of 1.388 eV. However, a similar isomer for AuO_2^- is much higher in energy with a triplet electronic state (C_s , $^3A''$). More importantly, it is predicted that Au^- and O_2 is unbound (Table 1). These theoretical predictions are consistent with the experimental observations; that is, no $\text{Au(O}_2\text{)}^-$ isomer was observed for AuO_2^- , but a $\text{Au(S}_2\text{)}^-$ isomer was indeed observed for AuS_2^- (Figure 4). The calculated first VDE (2.282 eV) for the $\text{Au(S}_2\text{)}^-$ isomer is in excellent agreement with the experimental measurement (2.24 ± 0.03 eV). Although the $\text{Au(S}_2\text{)}^-$ isomer is higher in energy than the linear

Scheme 1

AuS_2^- global minimum by 0.568 eV, the dissociation from the singlet $\text{Au(S}_2\text{)}^-$ to Au^- (1S) and S_2 ($^3\Sigma_g^-$) or isomerization to SAuS^- ($^3\Sigma_g^-$) is spin forbidden. Thus the observation of the $\text{Au(S}_2\text{)}^-$ isomer in our experiment should be mainly due to kinetic reasons.

4.2. AuO^- and AuS^- . The spectral assignments and comparisons between experimental and computed VDEs for AuO^- and AuS^- are given in Tables 4 and 5, respectively. The ground state of AuX^- was predicted to be $^1\Sigma^+$ with a closed-shell electron configuration: $1\sigma^2\pi^4\delta^42\sigma^2\pi^{*4}$ (Scheme 1). Pictures of these MOs for AuO^- and AuS^- are shown in Figure 5. The 1σ , π , and δ MOs are primarily of Au 5d characters with contributions from the O/S p orbitals, whereas the 2σ and π^* MOs are mainly from the O/S p orbitals with contributions from the Au 5d and 6s orbitals. Photodetachment from the π^* HOMO of AuX^- produces the $^2\Pi$ ground state of AuX , corresponding to band X in the spectra of AuO^- (Figure 1) and AuS^- (Figure 3). The calculated VDEs and SO splittings for this detachment channel agree well with the experimental data (Tables 4 and 5).

The next major detachment channel is from the 2σ MO, resulting in the $^2\Sigma_{1/2}$ excited state for AuX . This corresponds to the intense A band in the spectra of AuX^- . The calculated VDE for this detachment channel (3.925 eV) for AuO^- is in excellent agreement with the experimental result (3.945 ± 0.020 eV), whereas the calculated VDE (4.242 eV) for AuS^- is slightly underestimated in comparison to the experimental result (4.402 ± 0.015 eV). As shown in Tables 4 and 5, there is a considerable configuration mixing in the $A^2\Sigma_{1/2}$ state, in particular in AuO , where there is a mixing of 38% from a $^4\Sigma_{1/2}$ state (10% in the case of AuS). A weak PES band (a) with a vibrational progression was observed at 3.745 eV in the 266 nm spectrum of AuO^- (Figure 1b). According to our calculation, the a band corresponds to a final state with considerable configuration mixing, with the dominating component coming from the $^4\Sigma_{1/2}$ state. The $^4\Sigma_{1/2}$ state derives from an MO configuration of $\pi^{*2}\sigma^{*1}$, i.e., a two-electron detachment transition (detachment of an electron from the π^* orbital and simultaneous excitation of a second π^* electron to the σ^* MO). Such two-electron transitions are forbidden in the single-particle approximation. But this transition in AuO^- gains intensity from the significant mixing of the $^2\Sigma_{1/2}$ state (36%, see Table 4). Interestingly, this two-electron transition is negligible in the spectra of AuS^- , in excellent agreement with the theoretical prediction that there is a very small mixing of the $^2\Sigma_{1/2}$ state (only 9%, see Table 5).

The next detachment channel occurs from the δ MO, resulting in the $^2\Delta$ final state and corresponding to the B band in the spectra of AuX^- . The calculated VDE (5.443 eV) for AuO^- is slightly overestimated relative to the experimental result (5.24

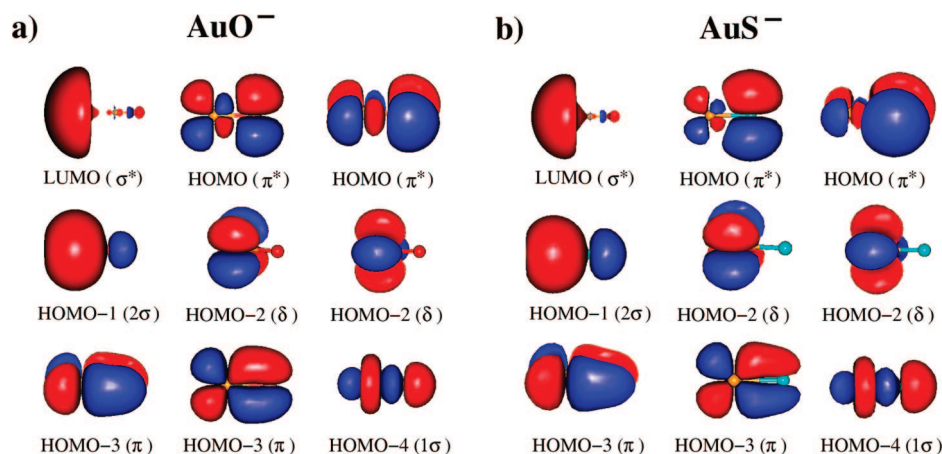


Figure 5. Molecular orbital pictures for (a) AuO^- and (b) AuS^- .

± 0.03 eV), whereas the calculated VDE (5.525 eV) for AuS^- is in quantitative agreement with the experimental result (5.54 ± 0.03 eV).

The next major detachment channels are from the π and 1σ MOs. Our calculations show considerable configuration mixing for these detachment channels in both systems (Tables 4 and 5). In the case of AuS^- , there was not enough signal-to-noise in the 193 nm spectrum (Figure 3c) to allow definitive resolution of individual states for these high binding energy detachment transitions. Our discussion focuses mainly on the AuO^- case, for which well resolved and rich spectral features were observed in the 193 nm spectrum in the high binding energy range (see inset in Figure 1c). The detachment channel from the π MO results in the $^2\Pi$ state, which can have a strong SO splitting. The calculations show that both SO states have major configuration mixings. The bands C and D at 5.72 and 5.97 eV each with a broad vibrational progression are assigned to the $^2\Pi_{1/2}$ and $^2\Pi_{3/2}$ states, respectively, with calculated VDEs of 5.818 and 6.111 eV, in good agreement with the experimental values. The detachment from the 1σ MO leads to the $^2\Sigma_{1/2}$ final state, which is assigned to the E band with a broad vibrational progression. The calculated VDE of 6.248 eV is in good agreement with the experimental value of 6.11 ± 0.04 eV. There are a number of weak features (*b–f*) between ~ 5 –5.5 eV, which are not assigned. They are likely due to multielectron transitions. Numerous multielectron transitions with extensive configuration mixings have indeed been predicted in these energy ranges (see Figure S2).

The broad vibrational progressions resulting from detachments from the 1σ and π MOs of AuO^- suggest they are strongly bonding orbitals, whereas our photoelectron spectra suggest the 2σ and π^* MOs are primarily nonbonding. This is a significant observation because it reveals directly the strong covalent nature and strong participation of the Au 5d orbitals in the Au–O bonding, as will be discussed further in section 5.

4.3. Linear AuO_2^- and AuS_2^- . The ground states of AuO_2^- and AuS_2^- were both predicted to have a linear XAuX^- structure with a triplet spin state ($D_{\infty h}$, $^3\Sigma_g^-$) and an open-shell configuration ($1\sigma_g^2 1\pi_g^4 \delta^4 1\sigma_u^2 2\sigma_g^2 1\pi_u^4 2\pi_g^2$), as shown in Figure 6. The pictures of the MOs for both AuO_2^- and AuS_2^- are shown in Figure 7. The $1\sigma_g$, $1\pi_g$, and δ MOs are primarily of Au 5d characters, and the rest are mainly of O/S p characters. The $2\pi_g$ HOMO is an antibonding MO, whereas the $1\pi_u$ MO is weakly bonding. The configurations of AuO_2^- and AuS_2^- are similar, except the ordering of the $1\sigma_u$ and $2\sigma_g$ MOs is

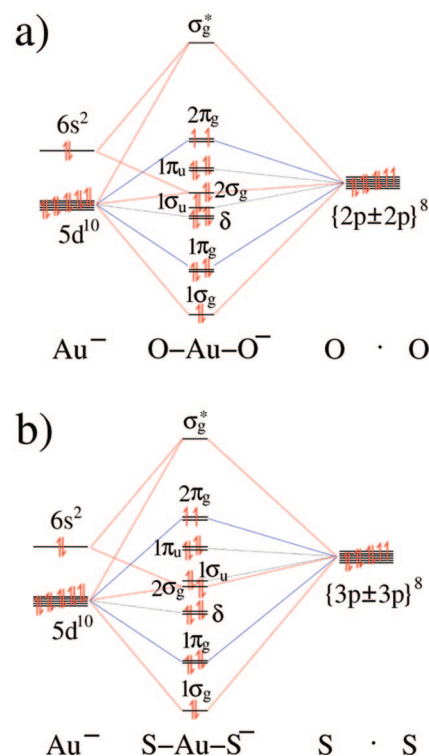


Figure 6. Molecular orbital diagrams for (a) OAuO^- and (b) AuS_2^- .

different in the two molecules (Figure 6). The open-shell anions allow both doublet and quartet final states to be reached via one-electron detachment, yielding more complicated photoelectron spectra. The spectral assignments and detailed comparisons between the calculated VDEs and experimental data are given in Table 6 for AuO_2^- and Table 7 for AuS_2^- .

Detachment from the $2\pi_g$ HOMO leads to the neutral $^2\Pi_g$ ground state of AuX_2 with a SO splitting ($^2\Pi_{g1/2}$ and $^2\Pi_{g3/2}$). The calculated VDEs for the transition to the $^2\Pi_{g1/2}$ ground state (3.473 eV for AuO_2^- and 3.468 eV for AuS_2^-) are in excellent agreement with the experimental measurements (3.40 ± 0.03 eV for AuO_2^- and 3.47 ± 0.03 eV for AuS_2^-). Because of the overlap of the $^2\Pi_{g3/2}$ SO state with the vibrational progression of the $^2\Pi_{g1/2}$ SO ground state, its VDE was not accurately determined. But the estimated VDEs for the $^2\Pi_{g3/2}$ SO state (3.60 ± 0.04 eV for AuO_2^- and 3.54 ± 0.04 eV for AuS_2^-) agree well with the theoretical results (3.627 eV for AuO_2^- and 3.585 eV for AuS_2^-). The substantial vibrational excitations

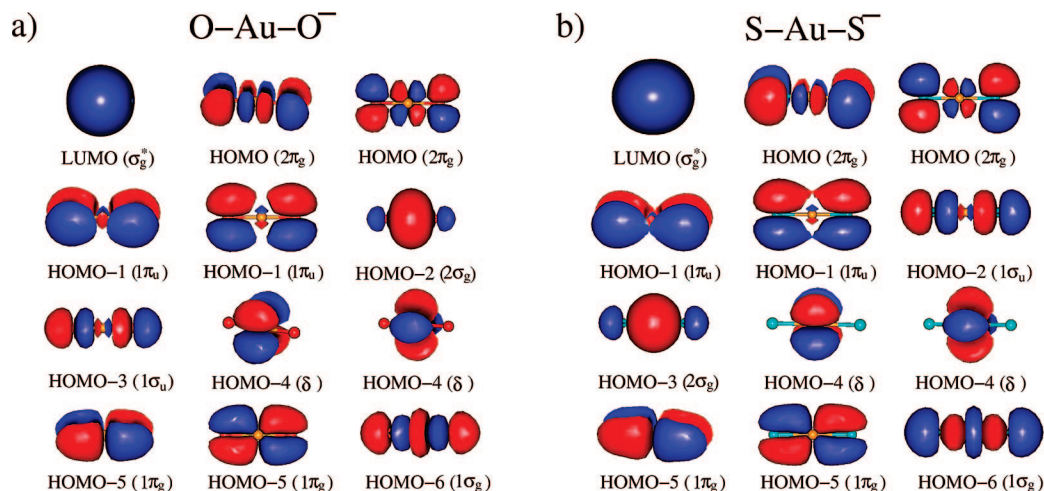


Figure 7. Molecular orbital pictures for (a) O-Au-O^- and (b) S-Au-S^- .

accompanying the detachment from the $2\pi_g$ HOMO in both AuO_2^- and AuS_2^- are consistent with the antibonding nature of this MO. This is also evident from the enhanced Au–O symmetric stretching frequency ($740 \pm 60 \text{ cm}^{-1}$) observed for the ground state of AuO_2^- relative to the AuO_2^- anion ground state ($\sim 600 \text{ cm}^{-1}$) estimated from the hot band transition.

The next detachment channel comes from the fully occupied $1\pi_u$ MO, which can lead to both quartet ($^4\Pi_u$) and doublet ($^2\Pi_u$) final states of AuX_2 . Both of these final states can have multiple SO components. The SO splitting for the $^4\Pi_u$ state ($^4\Pi_{u5/2}$, $3/2$, $1/2$, $-1/2$) was predicted to be very small in both molecules, ranging from 4.283 to 4.297 eV for AuO_2^- (Table 6) and 3.991 to 4.003 eV for AuS_2^- (Table 7). These SO splittings are smaller than our experimental resolution and thus could not be resolved in our experiment. The intense A band is assigned to the $^4\Pi_u$ state (Figures 2 and 4): the observed VDEs ($4.23 \pm 0.03 \text{ eV}$ for AuO_2^- and $3.96 \pm 0.03 \text{ eV}$ for AuS_2^-) are indeed in excellent agreement with the theoretical predictions. The short vibrational progression resolved for the $A^4\Pi_u$ state in AuX_2 suggests that the $1\pi_u$ MO has slightly Au–X antibonding character. The $^2\Pi_u$ state was predicted to have a more significant SO splitting. In the case of AuO_2^- , this prediction is in excellent agreement with the two weak PES bands at 4.70 and 4.78 eV (Figure 2), compared to the calculated VDEs, 4.713 and 4.785 eV (Table 6), for the $^2\Pi_{u1/2}$ and $^2\Pi_{u3/2}$ SO states, respectively. In the case of AuS_2^- , the predicted VDEs for the $^2\Pi_{u1/2}$ and $^2\Pi_{u3/2}$ SO states are 4.344 and 4.405 eV, respectively. However, in the photoelectron spectra numerous weak peaks were observed in the vicinity of these transitions due to spectral features from the $\text{Au}(\text{S}_2)^-$ isomer (see below). The two peaks at 4.35 and 4.40 eV were assigned to the $^2\Pi_{u1/2}$ and $^2\Pi_{u3/2}$ states based on the theoretical predictions.

The higher energy detachment channels become more congested, and the state ordering also becomes different for AuO_2^- and AuS_2^- according to the theoretical predictions. The observed spectral features can all be well assigned based on the theoretical predictions, as shown in Figures 2 and 4 and Tables 6 and 7 for AuO_2^- and AuS_2^- , respectively (see also Figures S4 and S5). It should be pointed out that detachments from the Au 5d based MOs ($1\sigma_g$, $1\pi_g$, δ) were predicted to occur at VDEs above 6 eV for both AuO_2^- and AuS_2^- and they were not observed due to the poor signal-to-noise ratios in the higher binding energy range at 193 nm.

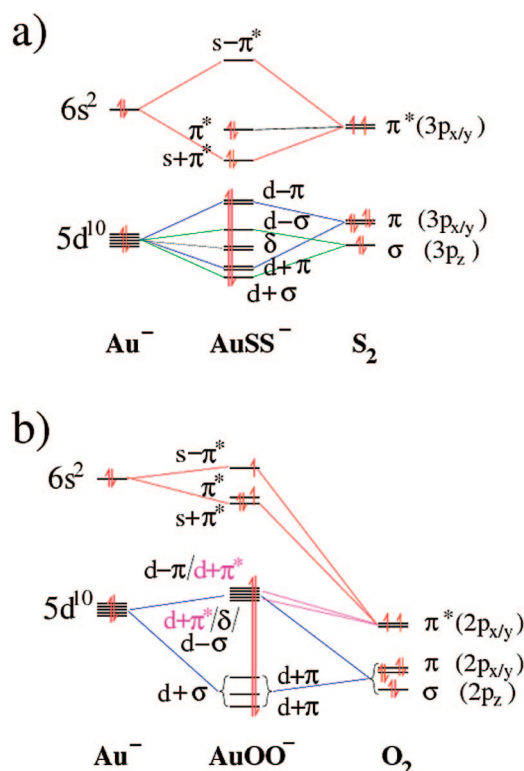


Figure 8. Molecular orbital diagrams for (a) AuSS^- and (b) AuOO^- .

4.4. $\text{Au}(\text{S}_2)^-$. Figures 8 and 9 show the MO correlation diagram and MO pictures of the bent $\text{Au}(\text{S}_2)^-$ isomer (C_s , $^1A'$). The corresponding figures for the unbound $\text{Au}(\text{O}_2)^-$ species (C_s , $^3A''$) are also shown for comparisons. Clearly the π^* HOMO of S_2 can interact favorably with the Au 6s orbital to form a strongly bound $s+\pi^*$ MO, a somewhat nonbonding MO (π^*) mainly localized on the S_2 fragment, and a strongly antibonding $s-\pi^*$ MO. The strong Au 6s and $\text{S}_2 \pi^*$ interactions result in a large separation between the bonding and antibonding MOs, leading to a closed-shell configuration for $\text{Au}(\text{S}_2)^-$. On the other hand, the unfavorable interaction between the Au 6s and the $\text{O}_2 \pi^*$ MO leads to an unbound $\text{Au}(\text{O}_2)^-$ with an open-shell configuration. The calculated detachment channels and spectral interpretations for $\text{Au}(\text{S}_2)^-$ are given in Table 8 (also see Figure S5). Detachment from the π^* HOMO of $\text{Au}(\text{S}_2)^-$

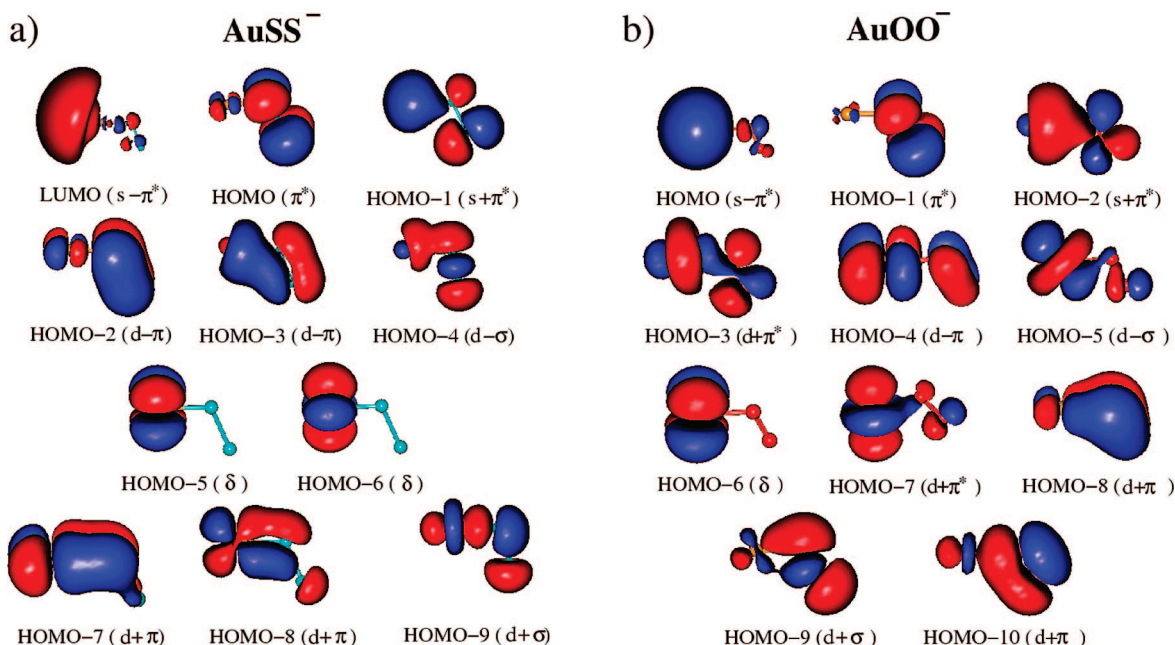


Figure 9. Molecular orbital pictures for (a) AuSS^- and (b) AuOO^- .

leads to the $^2A''$ ground state of neutral $\text{Au}(\text{S}_2)$. The observed vibration ($\sim 610 \text{ cm}^{-1}$) accompanying the ground-state detachment transition should be due to the S–S stretching, consistent with the fact that the HOMO is mainly localized on the S_2 unit (Figure 9).

The next detachment channel takes place from the $s+\pi^*$ bonding MO, resulting in the first excited state ($^2A'$) of $\text{Au}(\text{S}_2)$. The calculated VDE (3.013 eV) is in good agreement with the VDE of the A' band ($3.22 \pm 0.03 \text{ eV}$). The VDEs for the next two detachment channels were calculated to be at 4.355 and 4.634 eV, both with strong configuration mixings. The final states are designated with the major contributions as $^2A''$ and $^2A'$ and are assigned to the weak peaks at 4.27 eV (B') and 4.54 eV (C'), respectively (Figure 4 and Table 8). The next detachment channel was predicted to have a VDE of 5.473 eV, which would overlap with the $F^2\Sigma_u^-$ band of the linear AuS_2^- (Figure 4).

Overall the theoretical results are quite satisfying and allow quantitative interpretations of the experimental observations. Strong electron correlation effects were revealed in particular for the detachments from the AuX^- diatomics and the $\text{Au}(\text{S}_2)^-$ isomers, as can be seen from the contributions of basis sets to the final SO eigenstates in Tables 4, 5, and 8. The electron correlation effects are somewhat less pronounced for the detachments from the two linear AuX_2^- molecules at least for the low-lying transitions, which are dominated by single electron configurations.

5. Chemical Bonding in AuX^- and XAuX^- : O vs S

5.1. AuO^- vs AuS^- . The MO pictures for AuO^- and AuS^- are displayed in Figure 5. As shown in Scheme 1, the O(S) $p_{x/y}$ orbitals and Au $5d_{xz/yz}$ orbitals form the bonding π (HOMO-3) and antibonding π^* HOMO, which are both fully occupied in the anionic ground state. The O(S) p_z orbital interacts with the Au $6s$ and $5d_{z^2}$ orbitals to form the bonding 1σ (HOMO-4), nonbonding 2σ (HOMO-1), and the unoccupied antibonding σ^* LUMO, whereas the δ MO (HOMO-2) is purely nonbonding. The nonbonding nature of the 2σ and δ MOs in AuX^- is

confirmed by the photoelectron spectra, which show very little Franck–Condon activity upon electron removals from these MOs (Figures 1 and 3). On the basis of the MO configuration, the AuX^- molecules possess a single σ bond derived from the 1σ bonding MO because the bonding 1π and the antibonding π^* MOs cancel each other. However, while the strong bonding nature of the 1σ and 1π MOs are confirmed by the photoelectron spectra (strong Franck–Condon activities and the reduced vibrational frequencies in the C, D, and E PES bands of AuO^- , as shown in Figure 1c), the π^* MO is somewhat nonbonding as evidenced by the very weak Franck–Condon activities in the X bands (Figures 1 and 3). Thus, the AuX^- species contain some π bonding character. If the π^* MOs were completely nonbonding, the bond in AuX^- could be characterized as a triple bond. Indeed, the calculated bondlengths of AuX^- (Table 1) are only slightly smaller than the sums of the Au and X triple bond covalent radii proposed by Pyykkö et al. (1.76 Å for AuO and 2.18 Å for AuS).³³ Since the π^* MO does have some antibonding character, as evidenced by the stronger bonds in neutral AuX , the chemical bonds in AuX^- or neutral AuX are less than a triple bond. Removing all four π^* electrons would lead to a real triply bonded AuX diatomic species, which corresponds to the electron configuration of AuC^+ or AuSi^+ . Interestingly, these species have indeed been identified previously as containing a triple bond.³⁴

The Au–S bond is stronger than the Au–O bond in AuX^- , as indicated by their dissociation energies (Table 3): 2.677 eV for AuS^- vs 2.082 eV for AuO^- . The stronger bond in AuS^- is also reflected in its shorter bond length. The calculated bond length of 2.216 Å for AuS^- is much closer to the putative AuS triple bond length of 2.18 Å than the 1.882 Å bond length of AuO^- to the putative AuO triple bond length of 1.76 Å. The stronger AuS^- bond can be understood as being due to the less antibonding nature of its π^* HOMO. As shown in Figure 5, the Au $5d$ contributions to the π^* HOMO is smaller in AuS^- than in AuO^- , leading to the stronger AuS^- bond. The smaller

(33) Pyykkö, P.; Riedel, S.; Patzschke, M. *Chem.—Eur. J.* **2005**, *11*, 3511.

(34) Barysz, M.; Pyykkö, P. *Chem. Phys. Lett.* **1998**, *285*, 398.

5d contributions to the π^* HOMO are also reflected in the smaller SO splitting in the $^2\Pi$ ground state in AuS (0.111 eV) than in AuO (0.152 eV).

5.2. OAuO $^-$ vs SAuS $^-$. The bonding in OAuO $^-$ and SAuS $^-$ is also very similar, as can be seen from their MOs in Figure 7. As shown in Figure 6, the O(S) $p_{x/y}$ orbitals interact with the Au(5d $_{yz}$, 5d $_{xz}$) orbitals to form the strong bonding $1\pi_g$ HOMO-5, the nonbonding $1\pi_u$ HOMO-1, and the antibonding $2\pi_g$ HOMO. The $2\pi_g$ HOMO is half-occupied, resulting in the triplet ground state for AuX $_2^-$ ($^3\Sigma_g^-$). The interactions of O(S) p_z with Au 6s and 5d $_{z^2}$ yield the strong bonding $1\sigma_g$, the bonding $2\sigma_g$, the weakly bonding $1\sigma_u$, and the antibonding σ_g^* LUMO. The antibonding character of the $2\pi_g$ HOMO is clearly revealed by the substantial Franck–Condon activities in the ground-state detachment transition (Figures 2 and 4) and the increased Au–X stretching vibrational frequency in the neutrals compared to the anions. The $1\pi_u$, $2\sigma_g$, and $1\sigma_u$ MOs are basically nonbonding according to the photoelectron spectra (Figures 2 and 4) since there is very little Franck–Condon activity upon electron removals from these orbitals. Thus, the Au–X bonding in AuX $_2^-$ should also have substantial multibonding characters.

Interestingly, the Au–X bond is significantly strengthened in AuX $_2^-$ compared to that in the AuX $^-$ diatomics, as seen in Table 1. In particular, the dissociation energy of 4.046 eV for AuO $_2^- \rightarrow$ AuO $^-$ + O is almost twice as large as the AuO $^-$ dissociation energy (2.082 eV for AuO $^- \rightarrow$ Au $^-$ + O). This enhanced Au–X bonding in AuX $_2^-$ is also reflected in their shortened Au–X distances. The enhanced Au–X bonding in AuX $_2^-$ is most likely due to the partially occupied $2\pi_g$ antibonding orbitals, as well as from the strong covalent bonding interactions between the Au 5d and O(S) p atomic orbitals embodied in the $1\sigma_g$ and $1\pi_g$ MOs (Figure 7). It is also interesting to note that even though the AuO $^-$ bond is slightly weaker than the AuS $^-$ bond, the Au–O bond in AuO $_2^-$ is actually stronger than the Au–S bond in AuS $_2^-$. This is due to the stronger Au5d and O 2p bonding overlaps, as can be seen in the $1\pi_g$ and $1\sigma_g$ orbitals (Figure 7a). Overall, the Au–O and Au–S bonds in the diatomic AuX $^-$ and linear XAuX $^-$ molecules are strongly covalent with multiple bond characters due to the bonding capacities of the Au 5d orbitals as a result of the relativistic effects.³⁵

6. Chemical Bonding in Au(X $_2$) $^-$: Au $^-$ Does Not Bond to O $_2$

6.1. Chemical Bonding in Au(S $_2$) $^-$. The MOs of Au(S $_2$) $^-$ are compared with those of Au(O $_2$) $^-$ in Figure 9. As shown in Figure 8, the antibonding π^* MO of S $_2$ is well separated from its bonding π and σ MOs. This separation of bonding and antibonding MOs in S $_2$ makes them well matched energetically to interact with the Au 6s and 5d orbitals, respectively. However, the interactions of Au 5d and S $_2$ (σ and π) result in equal numbers of σ - and π -bonding and antibonding orbitals. Therefore, these interactions contribute little to the net chemical bonding in Au(S $_2$) $^-$. The bonding in Au(S $_2$) $^-$ originates primarily from the strong Au 6s and S $_2$ π^* interactions, which lead to a σ -bonding orbital ($s+\pi^*$), a nonbonding π^* orbital, and an antibonding σ orbital ($s-\pi^*$). Because of the strong σ interactions, the antibonding $s-\pi^*$ orbital is much higher in energy, leading to the closed-shell electronic structure for Au(S $_2$) $^-$ (C_s , $^1A'$). The fully occupied π^* HOMO is mainly localized on the S $_2$ fragment, consistent with the S–S stretching

vibrational progression observed in the ground-state PES transition (X' in Figure 4). The A' band derives from detachment from the $s+\pi^*$ bonding orbital. The unresolved vibrational features in the A' band should consist of both Au–S stretching and Au–S–S bending vibrations according to the nature of the $s+\pi^*$ MO. The separation of ~ 1 eV between the A' and X' bands in the photoelectron spectra of Au(S $_2$) $^-$ (Figure 4 and Table 8) indicates qualitatively the strength of the Au 6s and the S $_2$ π^* σ -interactions. The fact that this quantity is very close to the calculated binding energy (1.388 eV) of Au(S $_2$) $^-$ suggests that indeed the Au 6s and S $_2$ π^* σ -interactions are mainly responsible for the covalent bonding in Au(S $_2$) $^-$.

6.2. Au $^-$ Does Not Bond to O $_2$. As shown in Figure 8, the main difference in bonding between Au(O $_2$) $^-$ and Au(S $_2$) $^-$ is due to the orbital energy mismatch between Au $^-$ and O $_2$, resulting in little bonding interaction. This can also be seen quite clearly in the MO pictures of Au(O $_2$) $^-$ (Figure 9b). In particular, the weak interactions between the Au 6s and the O $_2$ π^* MO result in three closely lying frontier orbitals: $s+\pi^*$, π^* , and $s-\pi^*$ (Figure 8b), which is responsible for the open-shell configuration of Au(O $_2$) $^-$ ($^3A''$). Our calculations predict that at the chemical bonding distance Au(O $_2$) $^-$ is in fact repulsive with a negative dissociation energy (-0.272 eV), consistent with the MO analyses about the unfavorable interactions between Au $^-$ and O $_2$. Therefore, the Au $^-$ anion cannot chemisorb an O $_2$ molecule. This conclusion is consistent with the fact that no contributions from Au(O $_2$) $^-$ complexes existed in the AuO $_2^-$ spectra (Figure 2). We should point out that in a similar experiment on CuO $_2^-$ previously both a linear CuO $_2^-$ species and a Cu(O $_2$) $^-$ complex were observed.³⁶ Thus, the failure to observe Au(O $_2$) $^-$ was not due to experimental conditions but was rather an indication of the nonbonding nature between Au $^-$ and O $_2$.

The current observation is significant and relevant to the question of O $_2$ activation by gold clusters. It is generally believed that the activation of O $_2$ is the primary rate-limiting step in nanogold catalysis. Interestingly, even-sized Au $_n^-$ anion clusters were previously shown to react with O $_2$ primarily via charge transfer to superoxide-like Au $_n$ (O $_2$) $^-$ complexes, in which the dioxygen is activated but still molecularly chemisorbed on the Au clusters.^{10–14} However, odd-sized Au $_n^-$ clusters were shown not to react with O $_2$. This was well understood from the closed-shell electronic nature of the odd-sized Au $_n^-$ clusters, which makes it unfavorable for charge transfer to occur. The Au $^-$ anion is closed-shell and is the smallest odd-sized Au $_n^-$ species; thus its inactivity to O $_2$ is not surprising.

One interesting question is how the linear AuO $_2^-$ species are formed? In light of the nonbonding nature of the Au(O $_2$) $^-$ complex, it is not likely that it can be formed via dissociative chemisorption of O $_2$ on Au $^-$, as suggested previously.¹⁴ Furthermore, a barrier of more than 3 eV has been calculated for dissociation of O $_2$ on either a Au $^-$ anion or a neutral Au atom.¹⁴ There was evidence for the formation of neutral OAuO molecules in low temperature matrices via the reaction of AuO and O.⁵ Thus, the formation of the OAuO $^-$ molecule is most likely through reactions of gold atoms with an O atom in the cluster source to form AuO $^-$, which then reacts with another O atom to form AuO $_2^-$.

(35) Pyykko, P. *Chem. Rev.* **1988**, *88*, 563.

(36) (a) Wu, H.; Desai, S. R.; Wang, L. S. *J. Chem. Phys.* **1995**, *103*, 4363.
(b) Wu, H.; Desai, S. R.; Wang, L. S. *J. Phys. Chem. A* **1997**, *101*, 2103.

7. Conclusions

In conclusion, we report a combined photoelectron spectroscopy and *ab initio* study of monogold oxide and sulfide clusters: AuO_n^- and AuS_n^- ($n = 1, 2$). Well resolved photoelectron spectra were obtained for each species at various photon energies, providing a wealth of information on the low-lying electronic states of the corresponding neutral species. The spectra of AuO^- and AuS^- were found to be similar, but more spectroscopic information was obtained from the AuO^- spectra due to the high quality data. Specifically, a two-electron transition was observed in the spectra of AuO^- due to a shakeup process, and well resolved detachments from the Au 5d-based orbitals revealed strong Au 5d and O 2p covalent bonding. Whereas only a linear OAuO^- species was observed for AuO_2^- , both a linear SAuS^- and a bent AuSS^- isomer were observed for AuS_2^- . High-level *ab initio* calculations were performed to aid the interpretation of the experimental spectra, and the concerted experimental and computational data allow a complete understanding of the equilibrium geometries, electronic structure, and chemical bonding in the AuX^- diatomics and the AuX_2^- triatomic systems. Both strong spin-orbit coupling and electron correlation effects were found to be important to achieve good agreement between the calculated electron detachment energies and the experimental data. Comprehensive molecular orbital analyses were carried out to understand the chemical bonding in the AuX^- and AuX_2^- systems and to understand the

differences and similarities in the oxides vs sulfides. Strong covalent bonding was found in both the AuX^- diatomics and the linear XAuX^- species with multiple-bond characters. Interestingly, Au^- was shown not to bind molecular O_2 , whereas S_2 was found to bind Au^- by ~ 1.4 eV, in agreement with our experimental observations.

Acknowledgment. The experimental work was supported by the Chemical Sciences, Geosciences and Biosciences Division, Office of Basic Energy Sciences, U.S. Department of Energy (DOE) under Grant No. DE-FG02-03ER15481 (catalysis center program) and performed at the W. R. Wiley Environmental Molecular Sciences Laboratory, a national scientific user facility sponsored by the DOE's Office of Biological and Environmental Research and located at Pacific Northwest National Laboratory, operated for the DOE by Battelle. The theoretical work done in Berlin was supported by the German Science Foundation (D.F.G.). L.S.W. gratefully acknowledges the support of the Alexander von Humboldt Foundation, which makes this collaborative work possible.

Supporting Information Available: Complete ref 32, comparison of the 193 nm spectra of AuO^- and AuS^- , as well as AuO_2^- and AuS_2^- , and simulated spectra for AuX^- and AuX_2^- ($X = \text{O}$ and S). This information is available free of charge via the Internet at <http://pubs.acs.org>.

JA802408B